



# Experimental investigation of hypersonic flight-duplicated shock tunnel characteristics

C. K. Yuan<sup>1</sup> · Z. L. Jiang<sup>1,2</sup>

Received: 31 August 2020 / Revised: 30 September 2020 / Accepted: 25 October 2020 / Published online: 9 January 2021  
© The Chinese Society of Theoretical and Applied Mechanics and Springer-Verlag GmbH Germany, part of Springer Nature 2021

## Abstract

Hypersonic air-breathing propulsion is one of the key techniques for future aviation and the ground aerodynamic testing for full scale test models with sufficient test time at flight conditions is of fundamental importance for verifying hypersonic air-breathing engines. Based on the backward detonation-driven concept, the hypersonic flight-duplicated shock tunnel (or JF-12 shock tunnel) has been successfully constructed and calibrated. This facility is capable of reproducing airflow for Mach numbers ranging from 5 to 9 at an altitude of 25–50 km, with a test duration of more than 100 ms. To quantify the performance of the shock tunnel, experiments were conducted to investigate the aerodynamic characteristics of the test flows and the effects of several critical techniques that play important roles in the operation of the shock tunnel. The stagnation pressure was constant within  $\pm 5\%$  and the average stagnation pressure varied by less than 0.048%/ms. The variation of the stagnation pressure in repeated experiments is less than 2.0%, indicating the good repeatability of the wind tunnel. The non-uniformity of the Mach number in the core flow field at the nozzle exit was within  $\pm 2.5\%$ . Additional, a uniform flow field is established upstream of the nozzle exit. The axial gradients of the flow field are small since the Mach number varies less than 1.7%/m. Findings regarding the ignition technology, diaphragm ruptures, detonation driver capacity, incident shock-wave decay, and tunnel operation mode are also presented. The findings of this study are not only helpful for operating the shock tunnel, but can also assist the future development of hypersonic wind tunnels.

**Keywords** Hypersonics · Shock tunnels · Flow characteristics

## 1 Introduction

Hypersonic air-breathing propulsion can potentially reduce the cost of space access by using air from the Earth's atmosphere as an oxidizer. This allows for larger payload mass fractions, and increased flight maneuverability, and ensures routine access to space [1,2]. Although significant advances have been made over more than 60 years of research, major scientific and technological challenges prevent the development of practical hypersonic engines [3].

Ground propulsion testing is essential for understanding combustion flow physics, verifying engine techniques, and

predicting their flight performance. However, in the available facilities throughout the world, the testing capability is limited owing to scaled model testing, short test duration, and test flow contamination. Experiments are mostly being conducted on individual components, such as the inlet, fuel injection, and combustors. One of the most popular scaling laws for scramjet tests is pressure-length (PL)-scaling, which requires matching the product of a reference pressure and a flow field reference dimension. A smaller model scale requires faster reactions to ensure the validity of the simulation. If the flow temperature is correctly simulated, the combustion reaction rates mainly depend on the flow density. The binary reaction rates, such as dissociation, are linearly coupled with the flow density. However, for three-body reactions, such as recombination, the rates are quadratic in density. Thus, all combustion reactions can never be correctly simulated without a full-scale test model [4–6]. The consequences of incorrect simulation are as follows: (1) The final pressure achieved in the scramjet prior to the nozzle expansion is incorrectly scaled, which in turn influences the

---

Executive Editor: Jian-Qiang Chen.

✉ Z. L. Jiang  
zljjiang@imech.ac.cn

<sup>1</sup> Institute of Mechanics, Chinese Academy of Sciences, Beijing 100190, China

<sup>2</sup> University of Chinese Academy of Sciences, Beijing 100190, China

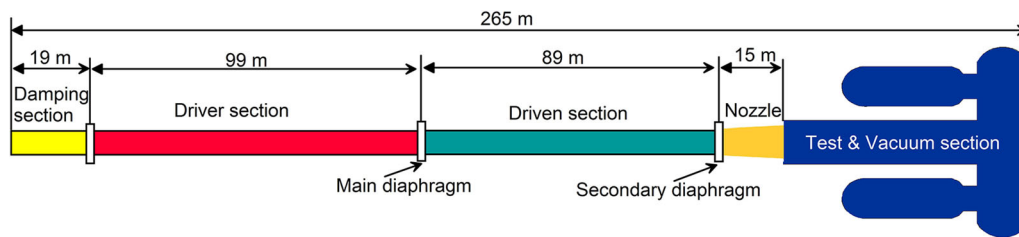


**Fig. 1** Schematic of the long-test-duration hypersonic detonation-driven shock tunnel

engine thrust. (2) The PL-scaling law does not preserve the equilibrium composition. Therefore, under chemical equilibrium conditions, static pressure changes affect the amount of heat released by combustion because more molecular species form at high pressures, which results in larger energy release. (3) The density increase associated with the pressure increase to compensate for the reduced length of a wind tunnel model implies that the flow approaches equilibrium at different test model positions. Although the effect on density is small, the stream-wise rate of the density variation is more severely affected, which may lead to small but important effects, such as a shift in the center of pressure [7,8]. Additionally, there is a strong coupling between the external flows of vehicles and the internal flow of hypersonic air-breathing engines. In conclusion, full-scale model testing is required to predict the engine performance accurately under flight conditions.

With regard to the above discussion, ground test facilities, which are capable of accommodating full-scale test models with sufficient test time under flight conditions, are required to gain reliable experimental results for hypersonic air-breathing vehicles. Three types of shock tunnels are widely used throughout the world for high-enthalpy flow generation. These facilities are light-gas-heated shock tunnels, free piston-driven shock tunnels, and detonation-driven shock tunnels. Among them, the detonation-driven shock tunnel is most promising with regard to achieving a lower cost-benefit ratio, simple structures, and long test duration [9]. Based on the backward detonation-driven concept, the hypersonic flight-duplicated shock tunnel (or JF-12 shock tunnel) has been successfully constructed and calibrated. This facility is capable of reproducing airflow for Mach numbers ranging from 5 to 9 at altitudes of 25–50 km with a test duration of more than 100 ms [10]. Specifically, the long test time of the shock tunnel is particularly useful for carrying out highly accurate force measurements with full-scale model.

In this paper, calibration results of the shock tunnel are presented to demonstrate its test flow performance and the effect of the key shock tunnel technology. This study is not only important for the operation of the shock tunnel and accurate analysis of experimental data, but also for developing future hypersonic flight-duplicated wind tunnels.

## 2 Facility and measuring instrumentation

### 2.1 Facility description

The hypersonic flight-duplicated shock tunnel is driven by detonation which has been successfully applied in shock tunnel and expansion tunnel [9,11]. The detailed techniques that have been developed to construct this facility can be found in Refs. [12,13]. The facility is capable of reproducing pure airflow with Mach numbers ranging from 5 to 9 at an altitude of 25–50 km, and an approximate test duration of 100 ms. Figure 1 shows a schematic configuration of the shock tunnel, which mainly comprises five parts. From left to right, the first part is the damping section with a length of 19 m and an inner diameter of 400 mm. The function of the damping section is to eliminate the excessive reflected pressure at the end of the driver section [14]. The initial pressure of the damping section should be as low as possible. Another advantage of the damping section lies in the fact that it can extend the time of the reflected wave arriving at the stagnation zone. The second part is the driver section with a length of 99 m and inner diameter of 400 mm. The driver section is filled with a detonable gas mixture. After ignition, a detonation wave propagates backward, while simultaneously launching a shock into the driven section. The actual driver gas is the detonation product. The driven section with a length of 89 m and inner diameter of 720 mm is connected with the driver section by the transient part, by which the inner diameter gradually increases. The experimental gas filled in this section is heated and compressed by the incident and reflected shock-wave. The next part is the contoured nozzle, which accelerates the experimental gas. Two nozzle sets are available. The larger one has a length of 15 m and exit diameter of 2.5 m, and can generate a flow field with Mach number of 7–9. The smaller nozzle has a length of 9 m and exit diameter of 1.5 m for Mach number of 5–7. When the smaller nozzle is used, the driven section should be prolonged from 89 m to 95 m. The last part is the test and vacuum section with an inner diameter of 3.5 m and total length of 43 m. The vacuum section adopts a E-shape to reduce the facility length caused by the space limitation of the Laboratory. Three test

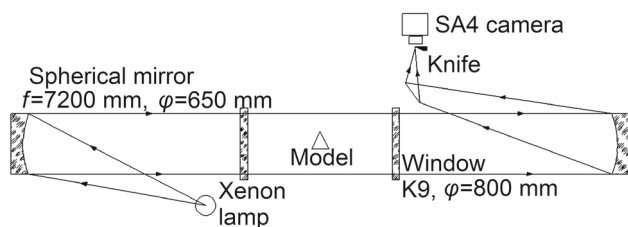


Fig. 2 Configuration of the schlieren system

conditions, shown in Table 1, were selected as the calibration test cases. Other test conditions appearing in the following sections were achieved by varying  $P_{4i}$ ,  $P_1$ , and the mole ratio of the detonable gas.

## 2.2 Measuring instrumentation

Piezoelectric and piezoresistive pressure sensors are mounted along the driver and driven sections. As piezoelectric sensors are sensitive to heating, they are used to measure the propagation velocity of the shock and detonation wave, whereas piezoresistive sensors are used to measure pressure values, such as the stagnation pressure, Pitot pressure, and model surface pressure values.

The flow field virtualization system was realized using a Z-type configuration schlieren, shown in Fig. 2. It mainly includes a light source coupled with a slit, two schlieren mirrors, lens, knife edge, and high-speed camera. The light source was a high-intensity xenon lamp in continuous mode. The displacement accuracy and moving range of the slit were 0.01 mm and 1 mm, respectively. In the optical set-up, two spherical mirrors with a diameter of 650 mm and focal distance of 7200 mm were used to collimate the light through the test section and focus it onto the knife edge. Dynamic schlieren images were captured using the Photron SA4 high-speed camera.

## 3 Effects of key technology

### 3.1 Ignition technology

Since the shock tunnel is driven by detonation, the direct initiation of detonation, as opposed to the transition from deflagration to detonation (DDT), is always needed to achieve a perfectly incident shock-wave in the driven section. Figure 3 shows the effect of the transition from deflagration to detonation on the stagnation pressure. The DDT induces unsteady stagnation pressure, and the stagnation temperature can not be obtained by solving the shock-wave relationship because the shock-wave structure in the driven section is too complex. Similarly, the free stream test flow param-

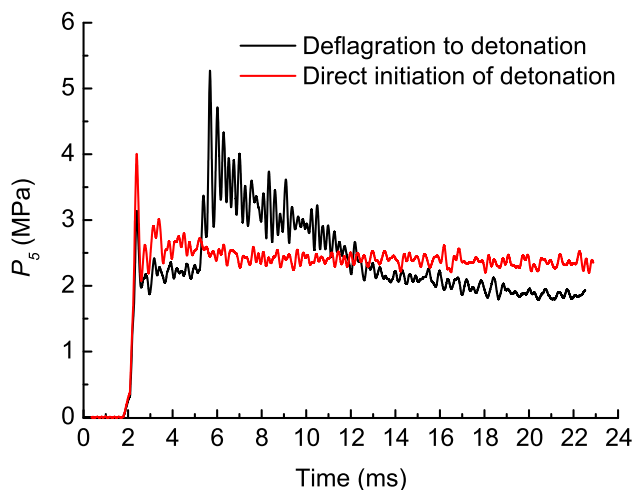


Fig. 3 Effect of the transition from deflagration to detonation on the stagnation pressure

eters are unknown. Thus, the DDT should be avoided in experiments.

The initiation of direct detonation is a key problem that prevents the development of detonation-driven shock tunnels. Previously obtained experimental results have revealed that the ignition energy must exceed a certain threshold. Additionally, this amount of energy for direct initiation depends on the mixture ratio of the given pressure, temperature, and igniter [15]. According to detonation theory, this means that the strong blast wave generated by a powerful igniter upon the rapid deposition of its energy decays asymptotically to the Chapman-Jouguet detonation. If the igniter energy is less than the critical value, the reaction zone becomes progressively decoupled from the blast as it decays, which results in deflagration [16]. For a large-diameter detonation driver and high initial pressure, the power required for the igniter is very high. In the laboratory, electrical explosion wire is one of the most low cost igniter. Experiments have been conducted to investigate the explosion process. Figure 4 shows the progress of explosion as captured by the high-speed camera. The imaging frame rate was 5000 fps and the exposure time was 200  $\mu$ s. As the electrical explosion is accompanied by radiation, we assumed that the gray scale of the image represents the energy generated by the electrical explosion wire. The derived normalized radiation intensity and radius are shown in Fig. 5. As can be clearly seen, the increase to the maximum ignition energy takes approximately 2.6 ms. The long increase time means that it is not feasible to initiate direct detonation by increasing the quantity of the electrical explosion wire. To solve this problem, a special ignition tube with a length of 1300 mm and inner diameter of 60 mm was manufactured and installed perpendicularly to the driver section. A stoichiometric mixture of hydrogen and oxygen was filled into the ignition tube

**Table 1** Calibration test case conditions

$H$ (km)	$Ma$	$P_{4i}$ (MPa)	$P_1$ (kPa)	$P_5$ (MPa)	$T_5$ (K)	$Re$ ( $m^{-1}$ )
33	6.0	1.5	19.0	1.53	1797	$1.35 \times 10^6$
35	7.0	2.7	24.3	3.28	2222	$1.23 \times 10^6$
50	8.5	1.5	4.5	1.78	3433	$1.54 \times 10^5$

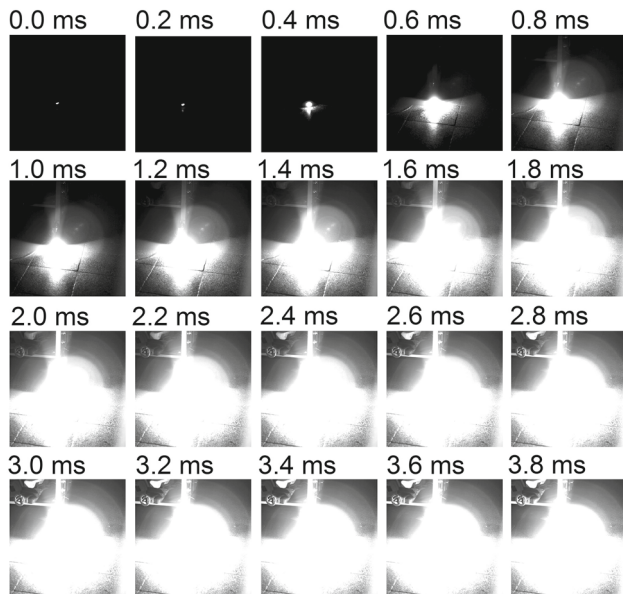


**Fig. 4** Measured explosion progress of the electrical explosion wire

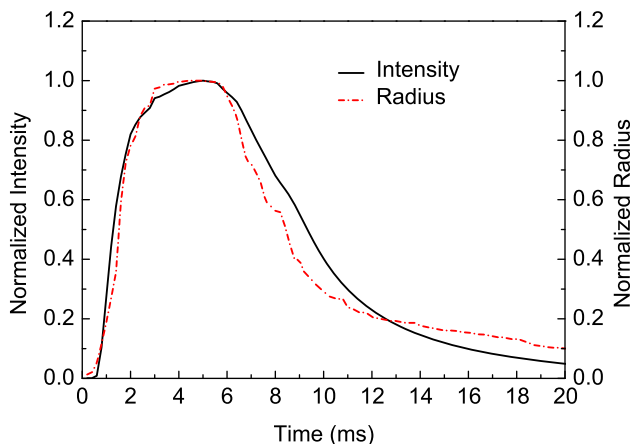


**Fig. 5** Derived normalized radiation intensity and radius

and ignited by the electrical explosion wire. The produced high-temperature gases were accelerated and injected into the driver section, and direct detonation was subsequently triggered in the driver section.

To confirm the ignition performance, three piezoelectric pressure sensors, labelled #1, #2, and #3, were mounted along the driver section to measure the pressure variation; the dis-

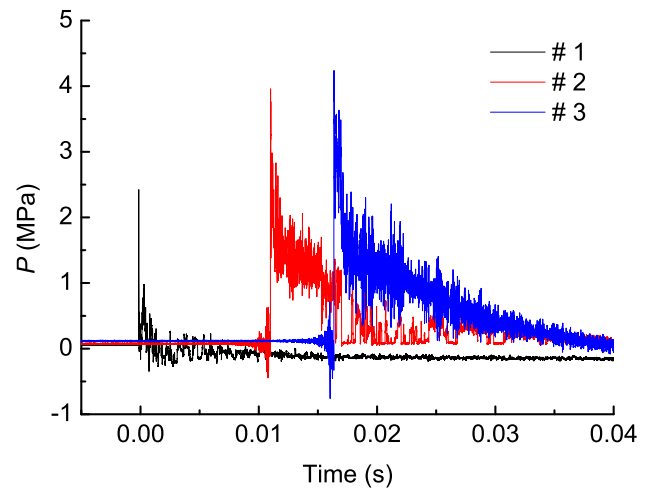


**Fig. 6** Typical output of the piezoelectric pressure sensors for measuring detonation wave velocity

tance of the sensors to the right end of the driver section was 90 mm, 25,522 mm, and 37,772 mm, respectively. Experiments were conducted under different operating conditions. Figure 6 shows the typical sensor output. The measured pressure profiles of sensors #2 and #3 clearly show the structure of the detonation front and combined Taylor expansion wave. The peak value of sensor #1 is lower compared with that of #2 and #3, mainly owing to the expansion wave generated by the rupture of the diaphragm. Then, the detonation wave velocity was calculated using the time of flight method. Table 2 presents the detonation wave velocity, where  $V_{12}$  and  $V_{23}$  denote the measured average velocity between sensor #1 and sensor #2, and the measured average velocity between sensor #2 and sensor #3, respectively. The theoretical detonation velocity was calculated with the help of Gaseq (a chemical equilibrium program developed by Chris Morlye, refer to [www.gaseq.co.uk](http://www.gaseq.co.uk) for detailed introduction). From Table 2, it can be confirmed that the average velocity  $V_{23}$  is approximately the same as  $V_{12}$ , which indicates a stably propagating detonation wave. As sensor #1 was installed at the ignition point, the constant velocity clearly indicates that direct detonation was in fact initiated in the driver section. Hence, the design of the ignition tube satisfies the experimental requirements.

**Table 2** Measured velocity of detonation wave in the driver section

Mole ratio	$V_{Theory}$	$V_{12}$	$V_{23}$
H <sub>2</sub> :O <sub>2</sub> :N <sub>2</sub> = 2:1:2.0	2296	2499	2501
H <sub>2</sub> :O <sub>2</sub> :N <sub>2</sub> = 2:1:3.6	2055	2276	2284
H <sub>2</sub> :O <sub>2</sub> :N <sub>2</sub> = 2:1:3.7	2048	2252	2279
CH <sub>4</sub> :O <sub>2</sub> :N <sub>2</sub> = 1:2:2.7	2148	2531	2574

**Table 3** Measured plain diaphragm rupture time (a 3.5 mm thick diaphragm, scored to 1.2 mm depth)

Run No.	$M_s$	$P_{4i}$ (MPa)	$P_1$ (kPa)	Time (ms)
08920	5.0	1.0	12.6	2.32
08921	5.0	1.0	12.6	2.22
08923	5.0	1.0	12.6	2.39
07923	5.0	1.5	19.0	1.64
08929	5.0	1.5	19.0	1.73
08912	5.0	1.5	19.0	1.68
08902	5.0	2.0	25.3	1.39
08930	5.0	2.0	25.3	1.38

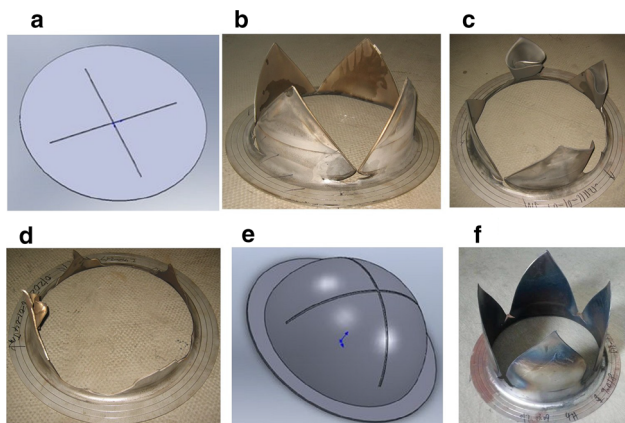


**Fig. 7** Main diaphragm. **a** Plain diaphragm. **b** Broken plain diaphragm ( $P_{4i} = 2.0$  MPa). **c** Broken plain diaphragm ( $P_{4i} = 2.5$  MPa). **d** Broken plain diaphragm ( $P_{4i} = 3.0$  MPa). **e** Spheric diaphragm. **f** Broken spheric diaphragm ( $P_{4i} = 3.0$  MPa)

### 3.2 Diaphragms

Three diaphragms, with the main diaphragm being the most important, separated the dumping section, driver section, driven section, and nozzle. The main diaphragm had a diameter of 400 mm and was placed at the right end of the driver section. An ideal diaphragm is one that sustains the initial pressure, and cleanly and quickly breaks under the pulse load of the detonation wave. Even small diaphragm pieces can greatly damage the nozzle throat and test model. Additionally, the diaphragm should be as thin as possible to reduce the pressure loss caused by the diaphragm rupture. These considerations place highly demands on the material. Based on previous experience, a scored groove can control the rupture process and prevent the dispersion of metal particles into the flow. Therefore, many experiments have been conducted to determine an appropriate material and scoring method in the equipment commissioning process.

In this study, ST14 cold rolled steel was selected owing to its good tensile property, and four petals were scored on one side of the diaphragm. The plain diaphragm, shown in Fig. 7a, was used under relatively low operation pressure. Figure 7b shows the broken diaphragm with an initial driver pressure of 2.0 MPa. After weighing, it was ensured that no fragments were produced during the rupture. When the initial driver pressure increased to 2.5 MPa, it was observed that

the diaphragm petals were bent backward by the detonation wave. However, no pieces broke off. The rupture time of the plain diaphragm was determined from the passage of the shock at the piezoelectric pressure sensor downstream of the diaphragm. Table 3 shows the measured rupture time of the plain diaphragm. The experiments were conducted with the same incident shock-wave Mach number, and the initial pressure of the driver section and driven section was varied. The average rupture time was 2.31 ms, 1.68 ms, and 1.385 ms, while the initial driver pressure was equal to 1.0 MPa, 1.5 MPa, and 2.0 MPa, respectively. The reason for this is that the detonation wave load increases when the initial pressure was higher.

With further increase of the initial driver pressure to 3.0 MPa, all four petals were detached from the diaphragm, as shown in Fig. 7d. This greatly limited the operation capability of the wind tunnel. The diaphragm fully opened when the petals were closely attached to the inner wall of the driven section, and turned by 90 degrees for the plain diaphragm. The reduced rupture time led to a higher diaphragm deformation rate and the material strength did not satisfy the new requirements. One way to lower the deformation rate is to reduce the turn angle of the diaphragm petals. Therefore, a spherical diaphragm was designed by Zhao [9], and manufactured. As shown in Fig. 7e, the steel sheet was pre-stamped to be a diaphragm with a spherical dome. Another advantage of the spherical diaphragm is that it can further decrease the stress at the root of the diaphragm. The broken spherical diaphragm is shown in Fig. 7f. The petals remained intact, which indicates that the spherical diaphragm performed well under the high initial driver pressure.

### 3.3 Loss of driving capacity caused by diaphragm rupture

To realize the desired flow field in the test section, the initial parameters of the driven and driver sections should be determined. One-dimensional isentropic expansion, nor-

**Table 4** Pressure loss due to diaphragm rupture

Run No.	Detonation H <sub>2</sub> :O <sub>2</sub> :N <sub>2</sub>	Diaphragm Nick depth (mm)	<i>M</i> <sub>s</sub>	<i>P</i> <sub>1</sub>	<i>P</i> <sub>4</sub> (MPa) Effective	<i>P</i> <sub>4</sub> ' (MPa) Detonation	Pressure loss (%)
08920	2:1:3.76	1.2	5.0	12.6	2.28	2.82	19.15
07923	2:1:3.76	1.2	5.0	19.0	3.46	4.26	18.78
08930	2:1:3.76	1.2	5.0	25.3	4.64	5.70	18.60
08407	2:1:2.75	1.0	7.1	6.0	4.56	6.07	24.88
08413	2:1:3.76	1.0	5.0	38.0	6.56	8.60	23.72
08420	2:1:3.76	1.0	5.3	18.0	4.31	5.70	24.39
06411	2:1:3.76	0.8	4.9	38.0	6.17	8.60	28.26
06409	2:1:4.00	0.8	4.7	41.0	6.10	8.46	27.90

mal shock-wave flow equations, and detonation theory are helpful in obtaining the initial parameters of the driver and driven sections. However, the driving pressure loss caused by diaphragm rupture cannot be theoretically calculated. Thus, experiments were conducted to overcome this problem. In the experiments, it was not possible to measure the effective driving pressure. An alternative method is to measure the incident shock-wave Mach number (*M*<sub>s</sub>) and calculate the effective driving pressure (*P*<sub>4</sub>) according to the shock-wave equations. The pressure loss ( $\Delta P$ ) is defined in Eq. (1)

$$\Delta P = \frac{(P'_4 - P_4)}{P'_4} \tag{1}$$

where *P*<sub>4</sub>' is the pressure of the detonation product.

The time-of-flight method was used to measure *M*<sub>s</sub>. Therefore, three piezoelectric pressure sensors were installed along the driven section, with the distances from the main diaphragm of 1952 mm, 8032 mm, and 14,112 mm. The diaphragm was a 3.5-mm thick plain diaphragm, with a nick depths of 1.2 mm, 1.0 mm, and 0.8 mm. The measured results are presented in Table 4. According to these data, the pressure loss was approximately 19% with nick depth of 1.2 mm, and increased to 28% when the nick depth was 0.8 mm, respectively. This dataset provides a theoretical basis for determining the facility's initial parameters.

### 3.4 Decay of incident shock-wave

The strength of the incident shock-wave in the driven section is a critical parameter for determining the properties of the stagnation zone. As viscosity and heat conduction can not be ignored, a boundary layer is formed along the wall of the driven section. An important consequence of this boundary is that it generates weak pressure waves which catch up with and attenuate the incident shock-wave [17]. Experiments were conducted to investigate this phenomenon. The incident shock speed was measured by piezoelectric pressure sensors that were flush-mounted along the wall of the driven

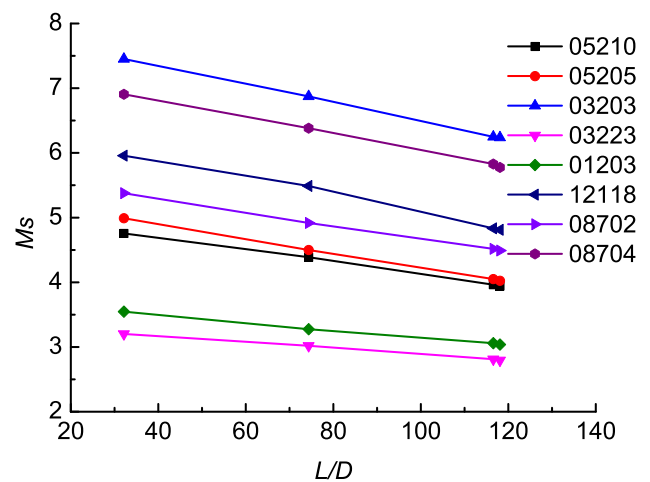


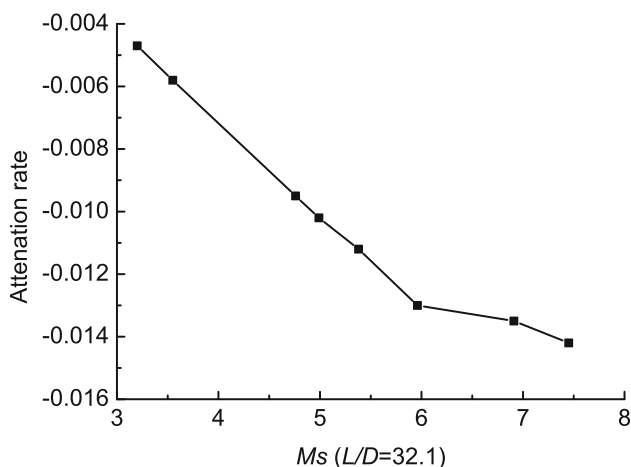
**Fig. 8** Measured incident shock-wave decay for eight test cases with different initial Mach number

section. These piezoelectric sensors had a full-scale range of 10 MPa, and a dynamic response frequency of 100 kHz. The output signals were simultaneously recorded by a multi-channel data acquisition system at 1.0 MHz per channel.

The experimental data of the incident shock-wave decay obtained for each of the eight test cases are presented in Fig. 8. The ordinate represents the Mach number of the incident shock-wave. The abscissa is *L/D*, where *L* is the distance to the main diaphragm and *D* is the diameter of the driven section. The data were further analyzed using the straight-line fitting method. Table 5 presents the fitting results and Fig. 9 shows the relationship between the attenuation rate and the Mach number of the initial incident shock-wave. The attenuation rate is defined as the Mach number drop per tube length nondimensionalized by the tube diameter. From the measured data, the following observations can be made: (1) The attenuation rate varies with the Mach number of the initial incident shock-wave. For example, when the initial incident shock Mach number was 7.45, 4.76, and 3.20, the calculated attenuation rates were −0.0142, −0.0095, −0.0047, respectively. (2) The adjusted coefficients of determination, which were

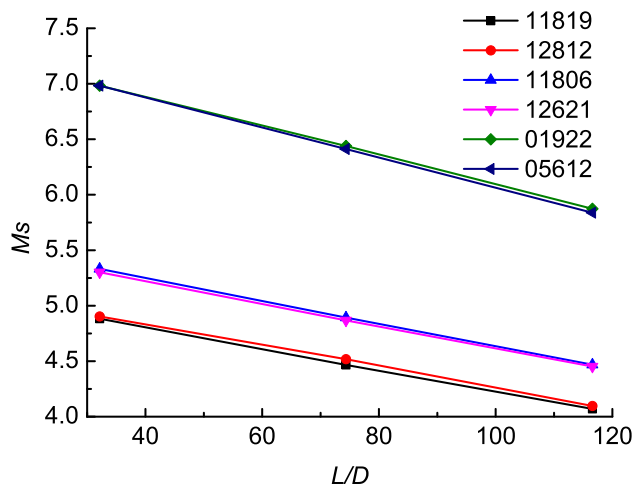
**Table 5** Fitting results of the data given in Fig. 8

Run no.	$M_s$ ( $L/D=32.1$ )	Attenuation rate	Adj. R-square
03203	7.45	-0.0142	0.9994
08704	6.91	-0.0135	0.9984
12118	5.96	-0.0130	0.9918
08702	5.38	-0.0112	0.9982
05205	4.99	-0.0102	0.9993
05210	4.76	-0.0095	0.9977
01203	3.55	-0.0058	0.9952
03223	3.20	-0.0047	0.9975

**Fig. 9** Attenuation rate variation with initial Mach number ( $L/D=32.1$ ) of the incident shock wave

obtained using the fitting method, were all greater than 0.99. This indicates that the attenuation rate along the driven section was approximately linear. (3) What stands out in Fig. 9 is that the attenuation rate obviously changed at  $M_s=5.96$ . This may have been caused by the high temperature gas effects, because the gas temperature behind the shock-wave was approximately 2000 K when the Mach number of the incident shock-wave was 5.96. The temperature was sufficiently high for causing chemical reactions and exciting the vibrational states of the molecules. As little information is known about the boundary layer, further investigation and novel measurement technology is required to elucidate the detailed mechanism.

The attenuation rate was further investigated while the initial pressure ratio was maintained in the driver and driven sections ( $P_{4i}/P_1$ ). The measured results are presented in Fig. 10. Table 6 summarizes the initial pressure, derived shock attenuation rate, and stagnation property ( $P_5$  and  $T_5$ ). The proportional change of the initial pressure of the driver and driven sections had a small effect on the attenuation rate and stagnation temperature, while the stagnation pressure proportionally changed. This is a useful finding because it

**Fig. 10** Measured incident shock wave decay while keeping  $P_{4i}/P_1$  constant

makes it very convenient to change the Reynolds number of the test flow field.

## 4 Flow field calibrations

### 4.1 Operation mode

After the rupture of the main diaphragm, an incident shock-wave propagated into the test gas in the driven section. Behind the incident shock, a contact surface followed and separated the driver and driven gas. The incident shock-wave was reflected at the end wall of the driven section, and created a region of almost stagnant, compressed, high-temperature gas.

After a short time, the reflected shock interacted with the contact surface. As shown in Fig. 11, during the interaction, new waves may be generated and propagate again downstream toward the end wall, while the reflected shock moves further upstream with changed velocity [18].

In the tailored mode, the conditions of the driver and driven gases at the interface are matched (or tailored), such that no additional waves are created by the interaction. The tailored mode is achieved by carefully controlling the pressure and the mixture of gases in the driver and driven sections [19]. The tailored mode is always desirable as it can effectively prolong the test time [20–22].

The stagnation pressure ( $P_5$ ) in the nozzle reservoir is an ideal parameter that indicates the operation mode. Additionally, the nozzle flow becomes more uniform when the stagnation is more stable. Figure 12 presents the measurement at the end of the driven section. These experiments were conducted at the stagnation temperature of 2205 K. From Fig. 12, the following observations can be made: (1)

**Table 6** Measured attenuation rate and stagnation property while keeping  $P_{4i}/P_1$  constant

	Run no.	$P_{4i}$ (MPa)	$P_1$ (kPa)	Attenuation rate	$P_5$ (MPa)	$T_5$ (kPa)
Case 1	11819	1.5	19.0	-0.0096	1.53	1797
	12812	0.75	9.5	-0.0096	0.68	1789
Case 2	11806	2.7	24.3	-0.0102	3.28	2222
	12621	2.0	18.0	-0.0101	2.40	2206
Case 3	01922	1.5	4.5	-0.0131	1.78	3433
	05612	2.0	6.0	-0.0136	2.41	3402

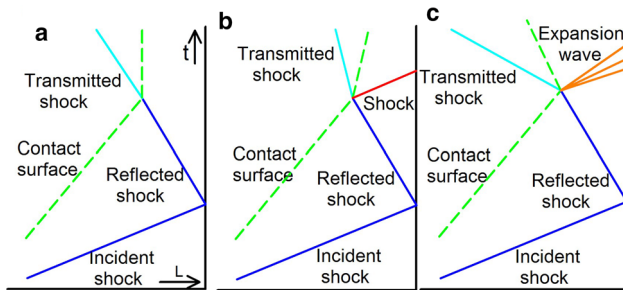


**Fig. 11** Interaction of the reflected shock with the contact surface. **a** Tailored mode. **b** Overtailored mode. **c** Undertailored mode

The quasi-tailored operation mode was successfully achieved in the hypersonic flight-duplicated shock tunnel. (2) Before the reflected detonation wave arrived at the end of the driven section, uniform pressure was maintained up to 130 ms. This time duration is sufficiently long, both for the flow pressure and heat transfer measurements, and for the hypersonic combustion and aerodynamic force measurements. (3) The stagnation pressure histories measured in the two experiments coincide with each other, which indicates the good repeatability of the shock tunnel. The average pressure of the two experiments, from 50 ms to 175 ms, was 3.06 MPa and 3.01 MPa. (4) The blue and purple dash dot lines indicate the constant value of 2.9 MPa and 3.2 MPa, respectively. From 50 ms to approximately 150 ms, the stagnation pressure varied between the lines, which means that the stagnation pressure was constant within  $\pm 5\%$ . Figure 13 shows the normalized stagnation pressure change ( $\frac{dP^*}{dt}$ ) derived from the measured pressure traces.  $P^*$  is the stagnation pressure normalized by

its average value. The two sharp peaks indicate the arrival of the incident shock-wave and the reflected detonation wave. During the test time, the average  $\frac{dP^*}{dt}$  was  $-0.048\%/ms$  and  $-0.044\%/ms$ .

Tailoring is theoretically possible only for one incident shock strength [23], which imposes a severe limitation to the capability of the shock tunnel. In practice, the overtailored mode and undertailored mode, which are respectively shown in Fig. 11b, c, are also useful driving methods if the reflected shock-wave or expansion wave becomes successively weaker within limited time. After multiple reflections, the reflections become sufficiently weak, such that temperature or pressure changes do not occur. The equilibrium temperature can be calculated by assuming that the reflections are isentropic, while the equilibrium pressure can be directly measured by a pressure sensor installed at the end of the driven section.

Figure 14 presents the comparison of the measured stagnation pressures of different operation modes. Each pressure curve in the figure was normalized with its average value. The following observations can be made: (1) In the undertailored mode and overtailored mode, it takes approximately 20 ms for a stagnation pressure to reach the equilibrium condition, with approximately 100 ms remaining for experiment. This means that untailored operation modes are acceptable in the hypersonic flight-duplicated shock tunnel. (2) The arrival time of the reflected detonation wave for the three operation modes was 176.8 ms, 179.6 ms, and 183.5 ms. Therefore, the operation mode only has a minor effect on the propagation process of the reflected detonation wave.

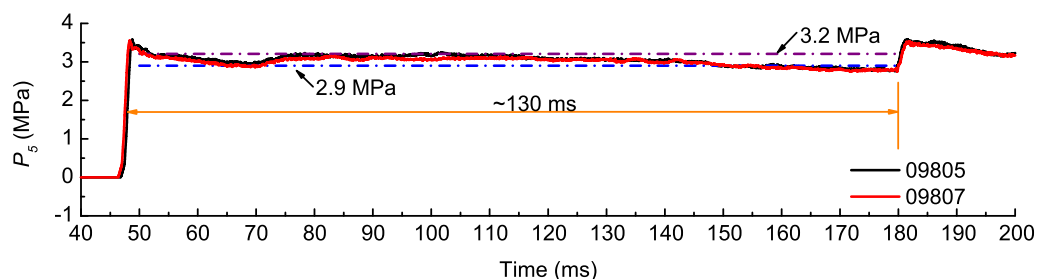


**Fig. 12** Stagnation pressure ( $P_5$ ) measured at the end of the driven section



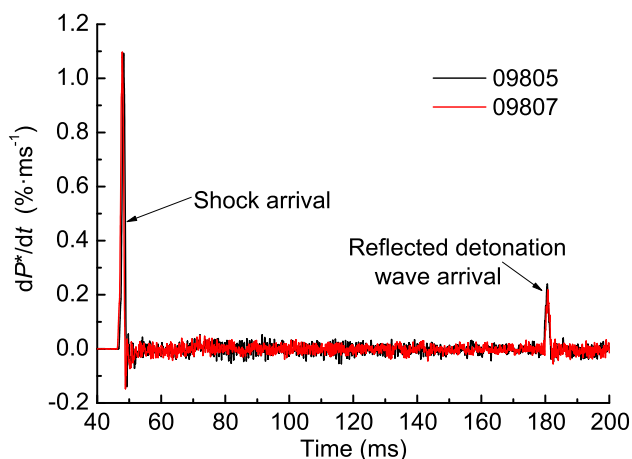


Fig. 13 Normalized stagnation pressure change

Notably, the measured steady stagnation pressure does not always indicate a uniform nozzle reservoir condition because the driver gas contamination changes the test gas properties. The mechanism for driver gas contamination has been reported in Refs. [24,25]. Although various methods and devices have been proposed to experimentally determine the driver gas contamination, most of them are ineffective in situations where detonation drivers are used, because the specific heat ratio variation caused by the contamination will be far less obvious [7,26]. Moreover, driver gas contamination is a great concern for reflected shock tunnels, and driver gas measurement experiments using laser absorption techniques are currently underway.

### 4.2 Nozzle flow

The steady flow duration at the test section is determined by the steady-flow duration at the nozzle reservoir, and also by the transient starting process of the nozzle. The transient starting process decreases the useful testing time of the tunnel, and an excessively long starting process severely limits its usefulness. Smith has pointed out that the transient flow conditions at a fixed nozzle location can be described as a function of time, as follows [27]: (1) No flow from the time of diaphragm rupture until the arrival of the primary shock-wave. (2) High-temperature, low-density flow between the primary shock-wave and the contact surface. (3) Low-temperature, higher-density flow between the contact surface and the secondary shock-wave. (4) Flow of increasing density as the expansion wave passes. (5) Final approach to the quasi-steady flow values. However, it is difficult to accurately measure the starting process as the opening process of the secondary diaphragm is unknown. Figure 15 shows the comparison of  $P_t$  with  $P_5$ . Notably,  $P_t$  was obtained at the probe located at the nozzle exit. From the figure, the following observations can be made: (1) The Pitot pressure at the nozzle exit follows the reservoir pressure with a time lag of approximately 5.3 ms. (2) It takes approximately 6.5 ms for the Pitot pressure to reach its peaks. This means that the flow reaches a quasi-steady state within 6.5 ms. Since the Pitot probe was designed with a particular structure to protect the sensor from the harsh flow, the time cannot be accurately measured.

Further experiments were conducted to measure the time required for the primary shock-wave to reach the nozzle exit.

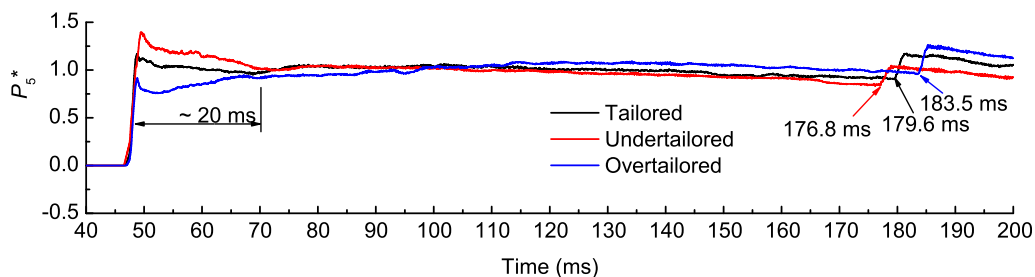


Fig. 14 Comparison of the measured stagnation pressure under different operation modes

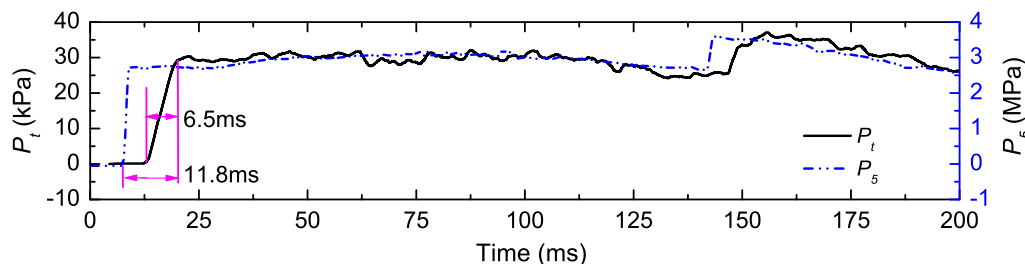


Fig. 15 Comparison of nozzle exit Pitot pressure  $P_t$  with reservoir pressure  $P_5$

**Table 7** Measured time required for the primary shock-wave to reach the nozzle exit

Run no.	Nozzle			$P_5$ (MPa)	$T_5$ (K)	Time (ms)
	Exit dia. (mm)	Length(mm)	Nominal $Ma$			
02426	1500	9000	6	2.5	1688	4.5
03405	1500	9000	6	3.9	1713	3.4
12425	1500	9000	6	2.5	2155	4.0
11427	1500	9000	6	2.5	2926	3.7
08302	2500	15000	7	2.2	2359	6.8
01407	2500	15000	7	2.5	2356	6.2
04327	2500	15000	7	1.7	2020	7.9
11314	2500	15000	7	1.7	2284	7.7
11318	2500	15000	7	1.8	3346	6.4

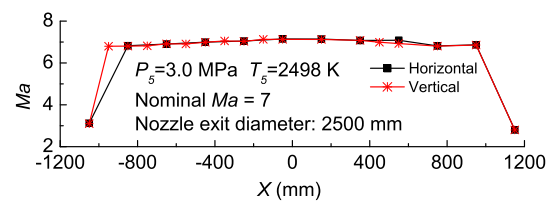
These results are valuable evaluating the numerical simulations for the nozzle flow. The experiments were conducted with two nozzle sets and nominal Mach numbers of 6 and 7. In the experiments, the nozzle and test sections were evacuated to 30 Pa. Table 7 presents the measured results. As can be seen, the increasing of the stagnation pressure or temperature accelerates the primary nozzle shock.

### 4.3 Flow field uniformity

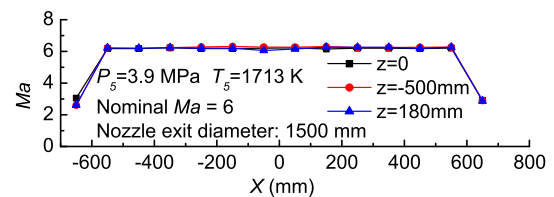
The flow field was calibrated using a cross Pitot rake. As the name suggests, this is a rake with two crossing arms carrying 40 spheres with a diameter of 24 mm. Each sphere is instrumented with a piezoresistance pressure sensor to measure the Pitot pressure at the stagnation point. The measured results are similar to those presented in Fig. 15. The Mach number profiles can be deduced from the measured Pitot and stagnation pressure.

Figure 16 presents the calibrated results for the larger nozzle. The nozzle exit diameter is 2500 mm and the nominal Mach number is 7. The experiments were conducted at the stagnation temperature of 2498 K and under a stagnation pressure of 3.0 MPa. From the figure, the following observations can be made: (1) The uniform core flow region at the nozzle exit plane has a diameter of approximately 2 m. Knowing the core flow region is helpful in determining the maximum size of the experimental model that can be tested without experiencing boundary layer effects from the tunnel wall. (2) The average value of the Mach number at the nozzle exit was 6.98 and the non-uniformity of the Mach numbers in the core of flow field was within  $\pm 2.5\%$ .

Figure 17 provides the measured Mach number profiles for the nozzle with an exit diameter of 1500 mm. Measurements were taken for three positions downstream of the nozzle: that is,  $z = -500, 0,$  and  $180$ . Here,  $z$  is a coordinate axis starting from the nozzle exit, and its positive direction coincides with the flow direction. For the smaller nozzle, the uniform



**Fig. 16** Mach number profile at the nozzle exit



**Fig. 17** Mach number profiles for three axial positions downstream of the nozzle

core flow region had a diameter of approximately 1.1 m. The Mach number profiles measured for the three positions only exhibited minor differences. In the central part of the flow field, the Mach number slightly varied as  $z$  increased. The average Mach number for the three positions was 6.26, 6.21, and 6.19. The variation of the Mach number is less than 1.7%/m. These results also indicate that a uniform flow field had already been established upstream of the nozzle exit.

Schlieren pictures provide a different method for visualizing and calibrating the flow field. A simple standard model was used in the calibration. The model was a sharp cone with a semi-vertex angle of  $10^\circ$  and axial length of 1500 mm, and was positioned in the test section with an attack angle (AOA) of  $5.2^\circ$ . The schlieren knife edge was set horizontally to obtain the vertical flow gradients. Figure 18 shows a typical schlieren image captured at the flow Mach number of 6.98. The free stream is from right to left. Shock-waves can be identified in the image. In particular, the windward shock can be seen owing to its high gray contrast. The images captured dur-

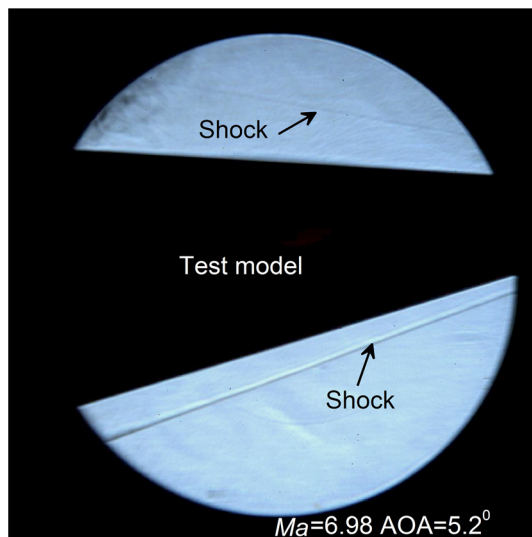


**Fig. 18** Typical schlieren image of the flow around the cone model

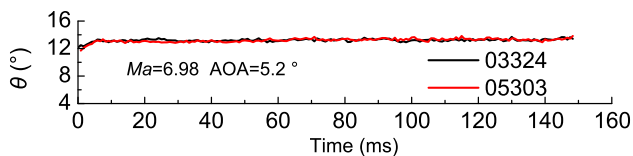


**Fig. 19** Extracted windward shock angle

ing the tests were further processed to extract the windward shock angle. Figure 19 shows the extracted windward shock angle ( $\theta$ ). From the figure, the following observations can be made: (1) The windward shock angles obtained from the two repeated experiments are identical, which also indicates the good repeatability of the flow field. The extracted shock angle was  $13.3 \pm 0.5^\circ$ . (2) The flow around the test model reached a quasi-steady state within approximately 4.5 ms. (3) The uniform stagnation pressure was maintained for approximately 130 ms, while the windward shock angle remained constant for at least 150 ms. This explains why the proposed methods for driver gas detection by variation of the shock angle during the contamination are not practical in detonation driven shock tunnels.

## 5 Conclusion

This study confirmed the successful development of the JF-12 shock tunnel by performance experiments, and obtained very encouraging results. This large-scale hypersonic flight-duplicated shock tunnel offers a large coreflow, sufficient test time, and pure air test conditions that are suitable for hypersonic scramjet vehicles. The following conclusions were drawn with regard to the facility's performance: (1) Tailored interface operation can be achieved in the Hypersonic Flight-

duplicated shock tunnel. The uniform stagnation pressure was maintained for as long as 130 ms, which is sufficient for hypersonic combustion tests. The stagnation pressure was constant within  $\pm 5\%$  and the average  $\frac{dP^*}{dt}$  varied by less than 0.048%/ms. (2) The variation of the stagnation pressure in repeated experiments is less than 2.0%, indicating the good repeatability of the wind tunnel. (3) The uniform core flow region for the big and small nozzle was 2.0 m and 1.1 m, respectively. The non-uniformity of the Mach number in the core flow field at the nozzle exit was within  $\pm 2.5\%$ . Additional, a uniform flow field had already been established upstream of the nozzle exit. The axial gradients of the flow field are small since the Mach number varies less than 1.7%/m.

The additional findings of this study are as follows: (1) The combination of an ignition tube with an explosion wire can initiate direct detonation in the driver section. (2) By increasing the initial pressure of the driver section, the rupture time of the main diaphragm was reduced. The reduced rupture time led to a higher diaphragm deformation rate and most of the material could not satisfy the requirements. Under these circumstances, the scored spherical diaphragm is a good choice for ensuring that pieces do not break off during the experiment. The diaphragm should be as thin as possible to reduce the driver pressure loss. (3) The incident shock-wave decayed linearly along the driven section. The attenuation rate varies with the Mach number of the incident shock-wave. Additional, the attenuation rate sharply changed at approximately  $Ms=6$ , possibly owing to high temperature effects. (4) Remarkably, untailed operation modes are also acceptable in the Hypersonic Flight-duplicated shock tunnel because it only takes approximately 20 ms for the stagnation pressure to reach the equilibrium condition, and 100 ms are still available for testing. (5) The Pitot pressure at the nozzle exit followed the stagnation pressure with a time lag. An increase in the stagnation pressure will accelerate the primary shock in the nozzle, and will result in a reduced time lag.

**Acknowledgements** This work was supported by the National Natural Science Foundation of China (Grants 11602275 and 11532014). The authors would like to acknowledge all the staff members in the shock and detonation physics group for their invaluable support.

## References

- McGilvray, M.: Comparison of Mach 10 scramjet measurements from different impulse facilities. *AIAA J.* **48**, 1647–1651 (2010)
- Van Wie, D.M.: Hypersonic airbreathing propulsion. *Johns Hopkins APL Tech. Dig.* **26**, 430–436 (2005)
- Hannemann, K.: Methodology of a combined ground based testing and numerical modelling analysis of supersonic combustion flow paths. *Shock Waves* **20**, 353–366 (2010)

4. Hornung, H.G.: Ground testing for hypervelocity flow, capabilities and limitations, Tech. Rep. ADA581905, California Institute of Technology (2010)
5. Pulsonetti, M.: A study of scramjet scaling. In: Proceedings of Meeting, Norfolk, November 18–22 (1996)
6. Karl, S.: CFD investigation of scaling laws for hydrogen fuelled scramjet combustors. In: Proceedings of Meeting, Versailles, November 3–6 (2008)
7. Gu, S.: Capabilities and limitations of existing hypersonic facilities. *Prog. Aerosp. Sci.* **113**, 100607 (2020)
8. Stalker, R.J.: Modern developments in hypersonic wind tunnels. *Aeronaut. J.* **110**, 21–39 (2006)
9. Zhao, W.: Performance of a detonation driven shock tunnel. *Shock Waves* **14**, 53–59 (2005)
10. Jiang, Z.L.: On theory and methods for advanced detonation-driven hypervelocity shock tunnels. *Natl. Sci. Rev.* **7**, 1198–1207 (2020)
11. Yuan, C.K.: Spectral measurements of hypervelocity flow in an expansion tunnel. *Acta Mech. Sin.* **35**, 24–31 (2019)
12. Jiang, Z.L.: Development and Calibration of Detonation-Driven High-Enthalpy and Hypersonic Test Facilities. Springer, Cham (2016)
13. Jiang, Z.L.: Theories and technologies for duplicating hypersonic flight conditions for ground testing. *Natl. Sci. Rev.* **4**, 290–296 (2017)
14. Yu, H.R.: Advances in detonation driving techniques for a shock tube/tunnel. *Shock Waves* **15**, 399–405 (2006)
15. Lu, F.K.: Recent advances in detonation techniques for high-enthalpy facilities. *AIAA J.* **38**, 1676–1684 (2000)
16. Ng, H.D.: Direct initiation of detonation with a multi-step reaction scheme. *J. Fluid Mech.* **476**, 179–211 (2003)
17. Mirels, H.: Attenuation in a shock tube due to unsteady-boundary-layer action, Tech. Rep., National Aeronautics and Space Administration. Lewis Flight Propulsion Lab (1957)
18. Olivier, H.: The Aachen Shock Tunnel TH2 With Dual Driver Mode Operation. Springer, Cham (2016)
19. Holden, M.S.: LENS Hypervelocity Tunnels and Application to Vehicle Testing at Duplicated Flight Conditions. American Institute of Aeronautics and Astronautics Inc, Reston (2002)
20. Amadio, A.R.: Test-time extension behind reflected shock waves using CO<sub>2</sub>-He and C<sub>3</sub>H<sub>8</sub>-He driver mixtures. *Shock Waves* **16**, 157–165 (2006)
21. Hong, Z.: Contact surface tailoring condition for shock tubes with different driver and driven section diameters. *Shock Waves* **19**, 331–336 (2009)
22. Wittliff, C.E.: The tailored-interface hypersonic shock tunnel. *J. Aerosp. Sci.* **26**, 219–228 (1959)
23. Copper, J.A.: Experimental investigation of the equilibrium interface technique. *Phys. Fluids* **5**, 844–849 (1962)
24. Boyce, R.R.: Mass spectrometric measurements of driver gas arrival in the T4 free-piston shock-tunnel. *Shock Waves* **14**, 371–378 (2005)
25. Goozee, R.J.: Simulation of a complete reflected shock tunnel showing a vortex mechanism for flow contamination. *Shock Waves* **15**, 165–176 (2006)
26. Chue, R.S.M.: Driver gas contamination in a detonation-driven reflected-shock tunnel. *Shock Waves* **13**, 367–380 (2003)
27. Smith, C.E.: An analytic study of the starting process in a hypersonic nozzle. Stanford University, Department of Aeronautics and Astronautics (1962). [Ph.D. thesis]

**Publisher's Note** Springer Nature remains neutral with regard to jurisdictional claims in published maps and institutional affiliations.